Contents lists available at ScienceDirect

Biochimica et Biophysica Acta

Molecular basis of endosomal-membrane association for the dengue virus envelope protein

CrossMark

David M. Rogers [1], Michael S. Kent, Susan B. Rempe *

Center for Biological and Materials Science, Sandia National Laboratories, Albuquerque, NM, United States.

ABSTRACT

Dengue virus is coated by an icosahedral shell of 90 envelope protein dimers that convert to trimers at low pH and promote fusion of its membrane with the membrane of the host endosome. We provide the first estimates for the free energy barrier and minimum for two key steps in this process: host membrane bending and protein–membrane binding. Both are studied using complementary membrane elastic, continuum electrostatics and all-atom molecular dynamics simulations. The predicted host membrane bending required to form an initial fusion stalk presents a 22–30 kcal/mol free energy barrier according to a constrained membrane elastic model. Combined continuum and molecular dynamics results predict a 15 kcal/mol free energy decrease on binding of each trimer of dengue envelope protein to a membrane with 30% anionic phosphatidylglycerol lipid. The bending cost depends on the preferred curvature of the lipids composing the host membrane leaflets, while the free energy gained for protein binding depends on the surface charge density of the host membrane. The fusion loop of the envelope protein inserts exactly at the level of the interface between the membrane's hydrophobic and head-group regions. The methods used in this work provide a means for further characterization of the structures and free energies of protein-assisted membrane fusion.

© 2014 The Authors. Published by Elsevier B.V. This is an open access article under the CC BY-NC-ND license (http://creativecommons.org/licenses/by-nc-nd/4.0/).

1. Introduction

Dengue virus (DV) is a flavivirus borne by mosquitos that causes flu-like symptoms and, in cases of secondary infection with a heterologous serotype, can lead to hemorrhagic fever. The virus is endemic to tropical regions, where it accounts for approximately 50 to 100 million infections and 500,000 hospitalizations annually [1]. The icosahedral envelope of the virus is made up of 180 identical copies of a single envelope (E) protein [2–5]. Two alpha helices anchored in the viral membrane attach to E through a 53-residue C-terminal stem [6]. Domain III, at E's C-terminus, helps the virus target cell receptors, leading to endocytosis [7–14]. Once inside the endosome, a low pH-driven conformational change of E results in exposure of hydrophobic residues at the tip of the beta-structured Domain II that attach E to the host endosomal membrane and promote virus–membrane fusion (Fig. 1) [15,16].

Recent experiments report that DV fusion with host endosomal membranes depends on the lipid composition of the endosome. The presence of cholesterol, on the one hand, substantially increases the fusion efficiency of viruses and virus-like particles with liposomes comprised of neutral lipids for tick-borne encephalitis [17,18] and West Nile flaviviruses [19], as well as Semliki forest virus (SFV), an alphavirus with an envelope protein homologous to E [20]. On the other hand, fusion of DV with the plasma membrane of insect cells (rich in anionic lipid) is independent of cholesterol [21]. Others report that fusion of DV is strongly promoted by the presence of anionic lipids in liposomes or host membranes [22]. These results raise questions about the factors that regulate E protein's binding and fusion efficiency, and in particular, the relative importance of anionic lipids and cholesterol.

Structural information for the E protein reveals that activation by low pH involves outward rotation of a primarily beta-structured Domain II relative to a 'base' Domain I/III located at the viral membrane surface [23]. This rotation exposes a large portion of Domain II to solvent, and triggers a conformational rearrangement from the 'smooth' dimeric shell of the mature virus (Fig. 1a) to 'spiky' trimeric assemblies of E protein on the virus surface (formed stepwise as in Fig. 1b and c). The rotation also leaves a fusion peptide (magenta in Fig. 1) exposed at the outer tip of the trimeric E protein assembly [5,6]. The E protein contains several positively charged residues on Domain II, resulting in substantial electrostatic attraction with negatively-charged membranes. The E protein fusion peptide consists of a short hydrophobic amino acid segment comprising residues 100–108. As confirmed by NMR and molecular simulation studies [24,25], hydrophobic residues, including tryptophan (Trp101) and phenylalanine (Phe108), promote

* Corresponding author.
E-mail address: slrempe@sandia.gov (S.B. Rempe).
[1] Current address: Department of Chemistry, University of South Florida, Tampa, FL, United States.
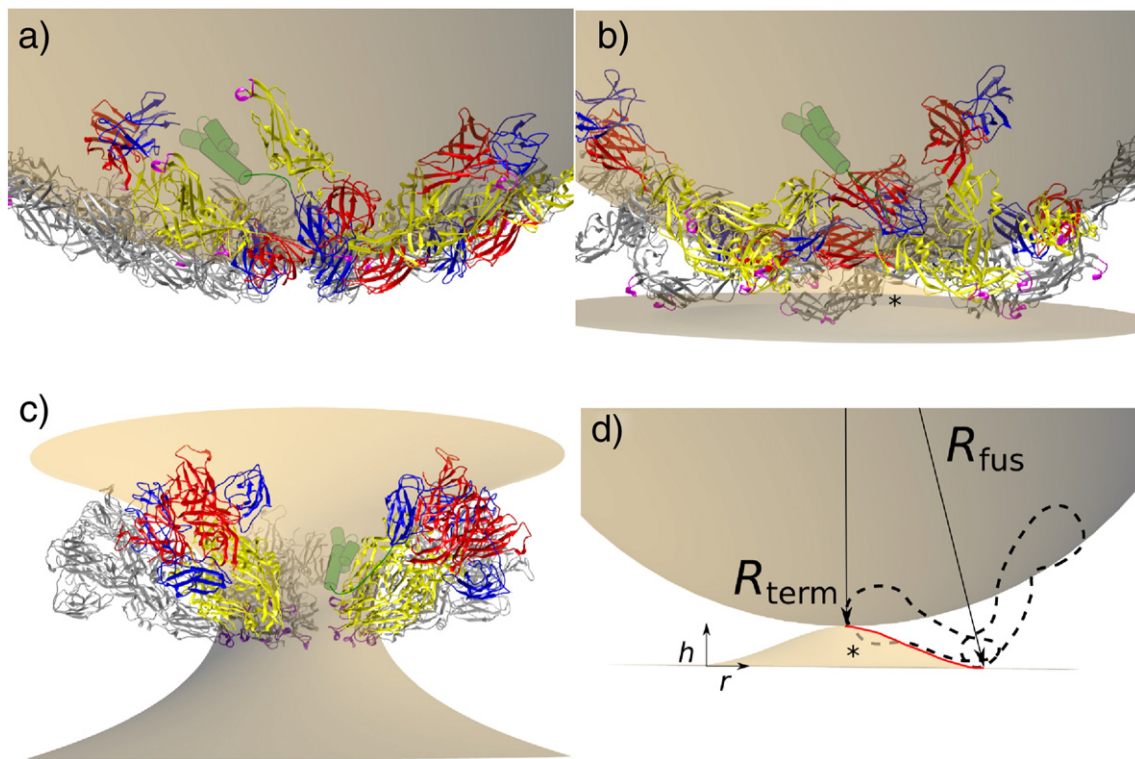
Fig. 1. Possible hemifusion route to virus (upper)–host (lower) membrane fusion, illustrated through alignment of E protein to: a) dimeric, mature viral assembly (3C6R [101]); b) an intermediate structure during trimerization approximated by the two cryo-EM structures with exposed fusion loops, 3C6D [101] and 3IXY [9]; c) target, fused state with trimeric form (1OK8 [6]) as proposed in earlier works [6,77], arbitrarily positioned to interact with a catenoid-shaped, zero mean curvature, membrane. Panels (b) and (d) are marked by * to illustrate the state defining the free energy barrier for this process. Panel (d) shows a red outline for the minimal energy dimple shape of the host membrane, $h(r)$, explained further in Fig. 2, and an outline of the 3IXY E protein structure used to constrain the host membrane shape. Two radii measured from the virus center identify the distance to the E protein fusion loop (R_{fus}) and N-terminal alpha-carbon (R_{term}). The actual conformation of the protein at steps (b–c), and the mechanism promoting the membrane dimple, are unknown. For clarity, only five trimers (i.e. from one pentagon in Fig. 2) are shown in (a)–(c), and the far three are colored gray. Protein domains I, II, III are colored (red, yellow, blue). Although not modeled in this work, the C-terminal stem and the perimembrane part of its anchor [5] are shown for reference (green) for one E monomer in (a)–(c). This stem region would sit between the E protein and the viral membrane. All E protein fusion peptides are colored magenta. Binding and conformational transitions of the fusion envelope protein may assist in lipid rearrangement or curvature formation during membrane fusion.

insertion of the E protein fusion peptide into the host endosomal membrane [26]. These structural insights do not contain energetic information required for comparison with existing models of the hemifusion process [27]. This study describes a method of obtaining reliable binding free energies that will be helpful for establishing the relative importance of cholesterol and anionic lipids.

In this work, we use atomistic and continuum-level simulations to present the first results on the membrane binding free energy of the E protein trimer. The potential of mean force (PMF) shows a broad minimum for viral protein–membrane association. Anionic lipids at 30 mol% concentration present a sufficiently strong attractive force on E protein to make this surface-associated protein–membrane contact irreversible. We also propose a transition state for the host membrane shape that puts an upper bound on the activation barrier to membrane bending needed to achieve membrane–membrane fusion. The host membrane composition can have a large influence on this barrier through its intrinsic curvature. The results reported here can be tested against experimental measurements of the protein-membrane binding free energy, E protein insertion depth, and dependence of binding and fusion on host membrane curvature.

The free energy barrier reported for fusion is an upper bound based on the geometry of initial host/virus contact. When attached at the largest membrane-facing face of the icosahedral viral envelope, the host endosomal membrane will simultaneously contact the fusion loops of five E protein trimers (Fig. 1b). The height and width of the E trimers present geometric bounds on this contact complex that are used to obtain energetic information. Because the barrier is determined

by mechanical constraints on the membrane, it specifies the amount of work that must be supplied by E to initiate fusion.

2. Theory

Building a detailed energetic picture of viral membrane fusion with endosomal membranes requires a combination of membrane elastic, dielectric continuum, and all-atom free energy methods. Membrane bending free energy models provide details on lipid rearrangements that take place on time-scales much larger than currently accessible with atomistic dynamics. Protein–membrane binding models provide details on atomistic rearrangements that take place locally and on short time scales. The E protein trimer measures roughly 10 nm in height and 7 nm wide at its base, on the viral membrane side, while the endosomal membrane adds an additional 4 nm in height, making full atomistic simulation challenging. By matching the all-atom and dielectric continuum potential of mean force curves for water-mediated protein-membrane interaction, we extend the all-atom results to complete separation, 3 nm from protein–membrane contact. The PMF value at complete separation establishes an absolute energy scale for the protein–membrane binding free energy.

2.1. Membrane bending free energy

The most widely accepted mechanism of spontaneous membrane fusion involves three major steps [27–30]. At first contact, the two membranes form an initial point connection (Fig. 1b and d). Next the

outer leaflets merge to form the so-called fusion stalk (Fig. 1c). Widening of the stalk leads to a hemifusion intermediate, defined by a single bilayer 'diaphragm' occupying a circular region in the plane separating the fusing vesicles. At this point, lipids from the outer leaflets of either membrane mix. This intermediate is favored when the outer leaflets contain lipids with negative intrinsic curvature, such as phosphatidylethanolamine (PE). In the final step of fusion, a pore forms in the hemifusion region to join the two vesicles, allowing mixing of the lipids on the inner leaflets and transfer of viral contents. This process is facilitated when the inner leaflets contain lipids with positive intrinsic curvature, including lysophosphatidylcholine (LPC). This mechanism of fusion explains the observed dependence of fusion kinetics on membrane composition in the absence of mediation by proteins [28].

A recent coarse-grained molecular dynamics study of unaided vesicle fusion confirmed stalk formation as the rate-limiting step [31]. Extensive simulations of the kinetics showed that the rate increased by an order of magnitude when changing the PC/PE lipid ratio from 2:1 to 1:1. In agreement with the curvature picture above, the authors also observed that increasing PE concentrations stabilized the hemifusion intermediate. As a side-effect, the long-lived hemifusion intermediate states slowed down the overall fusion kinetics. Simulations of coarse-grained membrane models gave estimates for the free energy barrier of around 13–18 kcal/mol for the initiation of fusion in small vesicles [30,32].

Since stalk formation presents the major free energy barrier to membrane fusion, reducing the barrier or supplying energy for membrane bending is a primary function of fusion-mediating proteins such as E. Because the largest component of this barrier comes from the elastic deformation of the membranes, elastic bending theory provides the most reliable measure for the activation barrier.

Prior works have used elastic theory to estimate the energy of the fusion stalk intermediate. Results have been variable due to differing treatments of the energy of the dimple formed by the inner leaflets and of void formation at the connection between the dimple and vertical walls of the stalk. For example, using toroidal and spherical shapes for the outer and inner leaflets to describe a 'dimple' [33] membrane shape within an elastic model, Kuzmin et. al. [34] found a free energy barrier of approximately 42 [35] to 132 [33] kcal/mol[2] exactly at a point where opposing membrane patches with radius $r \sim 1.4$ nm begin to merge. This barrier was lowered by 22 kcal/mol by finding the shape that minimizes the energy of the outer leaflets of the fusion stalk [35]. The dimple structure persists in the inner leaflets of membranes and forms the fusion stalk even after the outer leaflets have merged, contributing a free energy cost of 20 kcal/mol for a spherical dimple shape [35].

Formation of a fusion stalk also carries with it an associated hydrophobic void where the outer leaflet loses contact with the inner leaflet. The void free energy has received widespread attention [33,35,36], but lacks a firm quantitative basis. Recently, a near-quantitative model for the free energy of void formation in organic solvents (mimicking void formation in the aliphatic lipid tails) has become available [37]. A spherical void with 0.5 nm radius in bulk alkane liquid has a formation free energy of 10 kcal/mol at room temperature. For the membrane shape modeled in Ref. [35], the hydrophobic voids in the fusion stalk would be modeled more accurately with a 1 nm radius, but that would result in a void formation free energy that is so large as to be unphysical. Other studies [33,35,36] have considered cusped membrane shapes for the fusion stalk, with headgroup tilt on the inner leaflets. The tilted lipids fill all available space, removing the void formation free energy from consideration and resulting in a realistic free energy barrier for unassisted stalk formation (18–30 kcal/mol). Those models provide the current best estimates of the energy barrier to initial stalk formation during membrane–membrane fusion.

Since the bending free energy of the outer leaflet can be made nearly zero or even negative in curvature-based models of the fusion stalk (using catenoid-type shapes, shown in Fig. 1c) [35], the major contributor to the energy barrier will be the structure just before the fusion stalk, where both leaflets of the host membrane bend to form a dimple (Fig. 1b). In contrast to the work mentioned above, which focused on calculating the free energy of the fully formed fusion stalk (a metastable intermediate), the present calculation focuses on the (unstable) transition state. We also use a height and radius for the dimple structure determined by the arrangement of E protein trimers on the DV capsid membrane. Here, we predict the bending free energy barrier for formation of this transition state structure (Fig. 1b, d).

Because the viral surface places specific geometric constraints on the endosomal membrane dimple shape, we calculated membrane deformation energies using a free-form elastic model for the bilayer. The membrane shape is specified by the 2D surface of rotation for the function $h(r)$ — the membrane height as a function of radial distance from the dimple center (Figs. 1d and 2). The total work of deforming the membrane is then an integral over the energy density for each segment, dh, dr,

$$W^{\mathrm{bend}} = k_{\mathrm{bend}} \int_0^{R_{\mathrm{bound}}} s_E(r) 2\pi r \; dr. \tag{1}$$

R_{bound} is the outer boundary of the membrane deformation. The bending modulus of the host membrane, k_{bend}, determines the energy scale for the deformation. The bilayer energy density,

$$s_E(r) = (C_1 + C_2)^2 \sqrt{dr^2 + dh^2}/dr, \tag{2}$$

is computed from the square of the mean curvature of the host membrane along its two principal axes, $C_1 = d(\arctan(dh/dr))/dr$, and $C_2 = (dh/dr)/r$, following Ref. [35]. The Gaussian curvature ($C_1 C_2$) is assumed to make a minimal contribution since its integral is constrained following the Gauss–Bonnet theorem [38].

The shape boundaries are determined by the structure of the viral surface at the time of contact. The optimal shape for the remaining portions of the host membrane, $h(r)$, are found by numerically minimizing the free energy under these boundary constraints using the conjugate-gradient method. This approach determines an upper bound on the free energy barrier that must be overcome to form a dimple in the host endosome, just before it contacts the viral membrane.

To estimate this upper bound, we assume that the geometry for dimple formation is set by initial contact at an intermediate stage of the dimer to trimer transformation (Fig. 1b), before the trimer is fully formed with fusion loops extended. Similar contact geometries have been proposed in the literature [39,40]. Based on that assumption, we used the cryo-EM E structures 3C6D and 3IXY (Fig. 1b) to define the contact geometry. Domain II is only partially rotated outward in those structures of E protein. In contrast, crystal structures of the post-fusion state (Fig. 1c) show a fully formed trimer, after the protein conformational change driving fusion (Domain II rotation and zipping of the C-terminal stem loop) has already occurred [6]. The shape of the host membrane dimple found from the initial contact geometry represents a low-energy path for the protein tip to follow during E's dimer-to-trimer transition. Because the upper bound on the free energy determined in this work gives a feasible pathway to fusion, this assumed geometry for dimple formation is sufficient, but not necessary, for the E protein dimer-to-trimer transition.

2.2. Protein–membrane binding free energy

Binding of a viral fusion protein (E) to the host membrane will have further structural and energetic consequences. The binding free energy between protein and membrane may be calculated at different levels of approximation. The approximations are necessary due to both

---

[2] The uncertainty in Kuzmin's result is due to the fact that that work did not include an estimate for the free energy of forming the initial 'dimple' structure [33,36].
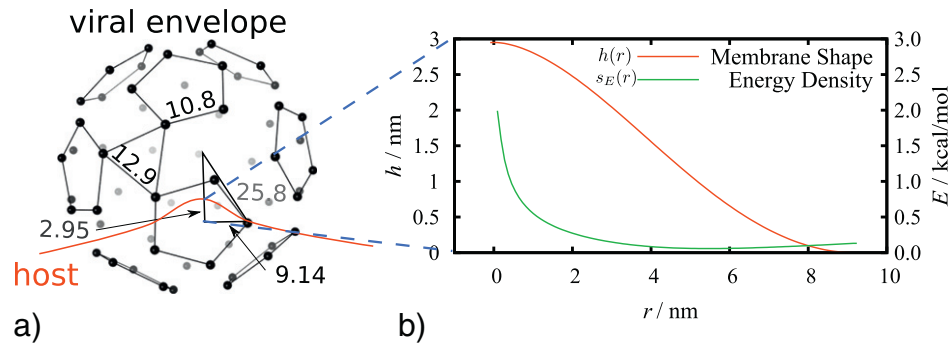
Fig. 2. Membrane shape and bending free energy (also shown in Fig. 1d). (a) The contact geometry of a pentagonal arrangement of E protein trimer on the viral membrane surface. Each black dot shows a cluster of three Phe108 alpha carbons from the fusion loop of the cryo-EM protein structure (PDB ID: 3IXY [9]). Distances are labeled in nm. (b) The host membrane shape that minimizes the bending free energy of a hemifusion intermediate in this contact geometry (red line sketched in (a)), shown for the contact distance of $R_{bound} = 9.14$ nm, where $W^{bend} = 30$ kcal/mol (Eq. (1)).

computational limits on the length of detailed simulations on the one hand, and inherent difficulties representing the potential energy surface with less detailed simulations on the other. At a coarse scale, Poisson–Boltzmann electrostatic plus surface term models [41], or pseudo-atom bead-based energetic models have been used. The surface terms approximate binding energies due to direct contact, and have been used to estimate orientations and binding free energy minima for a large class of membrane-associated proteins [42]. Coarse bead-based representations, such as the Martini force field [43], have been parameterized to reproduce water/membrane partitioning free energies for common amino acids. These models involve some fixing of the protein secondary structure, but can reproduce spontaneous assembly of lipid micelles and vesicles [43]. Although some progress has been made [44], most of these models do not yet treat electrostatics adequately,

which is required for distinguishing the effects of anionic vs. neutral membranes. United atom models take yet another step closer to all-atom dynamics simulations [45]. Even the detailed force fields of all-atom models, however, sometimes encounter difficulties in representing potential of mean force profiles [46,47].

In consideration of these challenges, we chose a two-scale approach to quantify the protein–membrane binding free energy as a function of separation distance. The membrane consisted of a homogeneous mixed bilayer enriched with 30% anionic lipid, 1-palmitoyl-2-oleoyl-*sn*-glycero-3-phosphoglycerol (POPG), with the remainder composed of neutral lipid, 1-palmitoyl-2-oleoyl-*sn*-glycero-3-phosphocholine (POPC). At large separations (> 1 nm), we calculated the interaction using a Poisson–Boltzmann electrostatic energy with a dispersion correction most accurate for those distances. Near contact (< 1 nm),
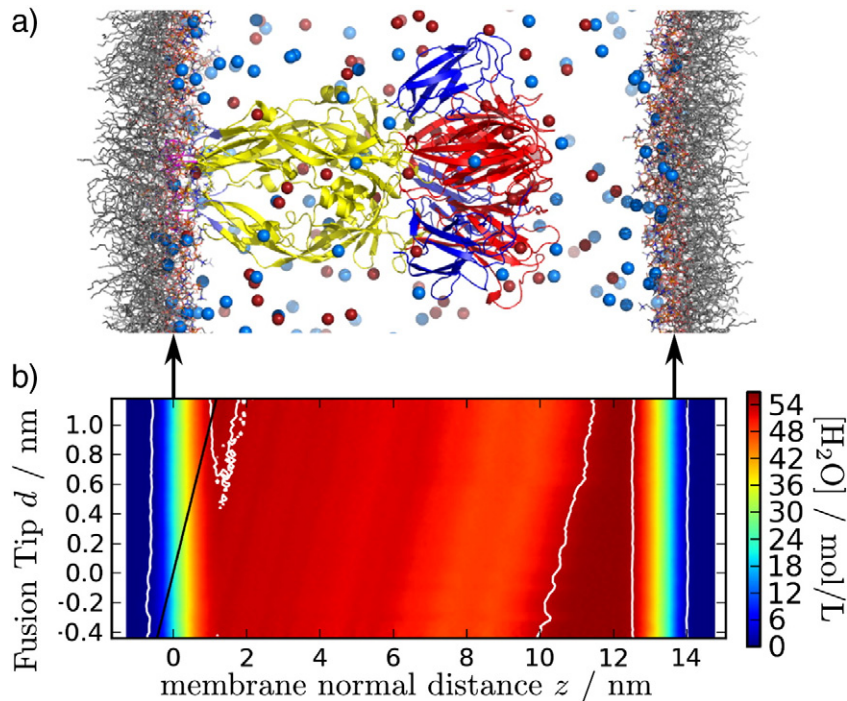
Fig. 3. Molecular model of the Dengue viral fusion protein trimer (E, 1OK8) during insertion into a homogeneous mixed endosomal membrane bilayer (7:3 POPC/POPG) represented in periodic boundary conditions. (a). Lipid carbons are shown in gray. Lipid head groups are colored (orange = phosphorous, red = oxygen, blue = nitrogen, white = polar hydrogen atoms). The protein representation is as in Fig. 1. Spheres indicate Na$^+$(blue) and Cl$^-$(red) ions in water (see Section 3.2.2 for further details). Panel (b) shows a series of water density profiles normal to the host membrane surface (z, same orientation as (a)). One density profile is plotted for each constrained separation distance, d, between the tip of the fusion protein and the membrane. The color scale indicates the water density in mol/L. A black line traces the center of geometry of the fusion loop as it moves leftward into the host membrane. White contours show the water density at 1 M (dark blue) and 54 M (dark red), indicating that the protein remains well separated from the membrane's periodic image throughout the simulation.

we also calculated the binding potential of mean force from all-atom molecular dynamics (MD) simulations (Fig. 3). This combination makes efficient use of two of the strongest methods available for computing potential of mean force curves for membrane–protein contact.

2.2.1. Continuum potential of mean force calculations

The continuum free energy, G^{conti}, is defined using only the interaction of particles with the mean field, ϕ_j, produced by the particle densities, $\{\rho_j\}$.

$$
G^{conti} = \frac{1}{2}\sum_j \int \rho_j(x)\phi_j(x) \; d^3x = G^{es} + G^{disp},
$$
$$
\phi_j(x) \equiv q_j\Phi(x) - c_3^j \sum_i \int \rho_i(y)c_3^i / max\left[(x-y)^2, R_0^2\right]^3 \; d^3y. \tag{3}
$$

The mean-field interaction terms for each atom type, j, were modeled using charge (q_j, contributing to the electrostatic component of the continuum free energy, G^{es}) and dispersion ($c_3^j \equiv \sqrt{2\epsilon_j R_j^3}$, contributing to the dispersion component of the continuum free energy, G^{disp}). Dispersion parameters are calculated from the Lennard–Jones well depth, ϵ_j, and minimum energy radius, R_j from the MD parameter set (Section 3). We used $R_0 = 0.2$ nm. Note that the energy is only sensitive to that parameter when the protein is within R_0 of the membrane.

The averaged electrostatic potential, $\Phi(x)$, was approximated by the solution of the linearized Poisson–Boltzmann equation,

$$
\nabla \cdot [\varepsilon(r)\nabla\Phi] - \left(\beta e^{-10\kappa(r)}\sum_i q_i^2 \rho_i^0\right)\Phi = -\rho_{ext}(r). \tag{4}
$$

The protein and membrane charge density were represented by $\rho_{ext} = \rho_p + \rho_m$, and the ionic charges (q) and bulk particle concentrations (ρ^0)

combine with the volume exclusion function in the ionic screening term. The volume exclusion function, $\kappa \in [0, 1]$, is defined as the larger of the membrane or protein volume exclusion functions, $max(\kappa_m, \kappa_p)$. We set the dielectric function, $\varepsilon(r)$, to 2 inside the membrane, 10 inside the protein, and 80 in bulk water [48]. The interfaces were described by a smooth combination of protein and membrane dielectric values: $\varepsilon_0 * ((10 - \varepsilon_m)\kappa_p + \varepsilon_m)$, with $\varepsilon_m = (2 - 80)\kappa_m + 80$, and ε_0 the vacuum permittivity.

Errors in this model are limited to large-scale protein and membrane shape changes or solvent and ion reorganization energies at large concentrations and voltages inconsistent with the linearized Poisson–Boltzmann approximation ($q\phi > k_B T$). For membrane–membrane interactions, hydration forces must be considered at separations closer than a few nm [49,50]. There, more accurate continuum interaction energies have been proposed [34,51]. Corrections for hydration forces and ionic effects in more concentrated environments form an important field of current research [50,52]. These errors are minimized in the present work by aligning the continuum and fully atomistic potential of mean force at 1 nm (Fig. 4).

The dispersion component of the potential of mean force between E and the endosomal membrane can be estimated using the coefficients in the pairwise-additive approximation of inter-atomic forces from the molecular dynamics simulations. For a uniform membrane density in the x–y plane, the protein–membrane interaction is

$$
G_{\alpha,\beta}^{disp} = -A \iint \frac{\pi\rho_3^{\alpha}(z)\rho_3^{\beta}(z')}{2max\left[(z-z')^2, R_0^2\right]^2} \; dz'dz, \tag{5}
$$

where R_0 is the distance of closest approach between protein and membrane atoms (α, β), A is the simulation area, and $\rho_3^{\alpha}(z) \equiv$
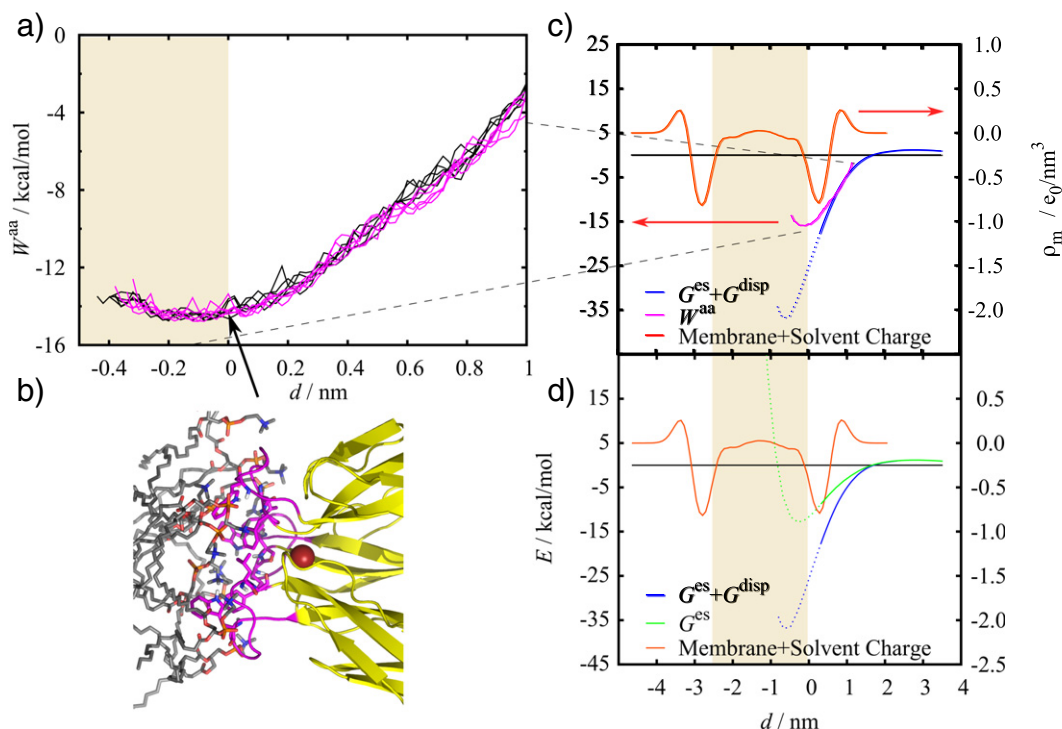
Fig. 4. Free energy as a function of E fusion loop-membrane glycerol separation distance. Panel (a) shows the convergence of the broad free energy minimum found with molecular dynamics to within 1 kcal/mol. There, separate PMF profiles were generated from 10 independent blocks of 0.525 ns each during sampling. Black and magenta colors belong to the first 5 and last 5 blocks, respectively. Panel (b) shows the contact region in a configuration chosen at random from the set of configurations at ~0 nm separation. The protein is on the right. Carbons on fusion loop residues (100–108) are colored magenta. A bound chloride ion (also present in the X-ray structure) is shown in red. The mixed membrane bilayer of neutral and charged lipids (7:3 POPC/POPG) (left) is colored as in Fig. 3(a). Panels (c) and (d) compare potentials of mean force computed from molecular dynamics simulations ($W^{aa}(d)$, purple lines) with those from continuum electrostatics and dispersion energy calculations ($G^{es}(d)$ and $G^{disp}(d)$, green and blue lines). Energy is given in units of kcal/mol (left axis). Panels (c) and (d) also show for reference the fixed charged density of the membrane, water, and ions, ρ_m (red lines, right scale). The tan columns highlight the membrane's hydrophobic interior.

$\sum_{j \in \alpha} \sqrt{2\epsilon_j R_j^6}\rho_{\alpha,j} - \sqrt{2\epsilon_w R_w^6}\rho_w$ is a volumetric density (plotted in the Supplementary material). The dispersion coefficient density of solution, ρ_3^w ($= 0.0216\sqrt{e}V$ in our calculations), must be subtracted since the protein and membrane are displaced by water and ions on translation.

2.2.2. All-atom potential of mean force calculations

Umbrella sampling was employed to compute the all-atom potential of mean force, $W^{aa}(d)$, as a function of vertical protein–membrane separation, d. A set of 50 simulations with harmonic biasing potentials centered at 0.3 Å intervals allowed sampling data from all separations in parallel. Monte-Carlo moves exchanging biasing centers between simulations were attempted every picosecond, with each exchange cycle attempting 125,000 swaps between neighboring bias centers. Those exchanges do not change the statistical properties of the equilibrium sampling, but speed equilibration time by ~ 3× compared to independent umbrella sampling simulations [53–55]. The speed-up is due to the ability of the replicas to diffuse along the constraint space, d. Data analysis was carried out by assigning weights w_i^j for each biasing potential, j, to each frame, i, using the multistate Bennett-acceptance ratio (MBAR) method [56]. An extra square-well containing the whole range of sampled d-values was added as $j = 0$ to computed unbiased averages. Appropriately unbiased conditional averages, $\langle f(x)|d(x) \in (d_1, d_2)\rangle$, were then computed for each protein–membrane separation distance range, (d_1, d_2), using

$$\langle f(x)|d \in (d_1, d_2)\rangle = \frac{\sum_i f(x_i)w_i^0 I(d_i \in (d_1, d_2))}{\sum_i w_i^0 I(d_i \in (d_1, d_2)}. \tag{6}$$

More advanced statistical methods can decompose molecular contributions near the surface into continuum and local contributions. For example, the brute-force computation of the potential of mean force carried out in this work could be refined using the ideas of Quasi-Chemical Theory [52,57–59]. There, the free energy of membrane–protein interaction can be expressed as a sum of the continuum calculations considered here and contributions from molecular packing and chemical solvation structures. That approach will be used in future work to study the dependence of the binding process on membrane composition and interfacial tension.

3. Methods

3.1. Membrane bending free energy

For the computation of W^{bend}, Eq. (1) was minimized to find the optimized shape of the endosomal membrane in contact with E protein on the outer viral surface determined by the 3IXY [9] and 3C6D [4] cryo-EM structures (as in Fig. 1d). The membrane deformation free energy was computed using 103 points equally separated in $r: -dr, 0, ⋯, 9.14, 9.14 + dr, 9.14 + 2dr$. Based on structure 3IXY, the boundary conditions consisted of: $h(-dr) = h(dr)$, $h(0) = 2.95$, $h(9.14 + dr) = h(9.14 + 2dr) = 0$. For 3C6D, this changed to $h(8.82 + dr) = 0$ and $h(0) = 2.38$. The resulting membrane shape, measured in nanometers (nm), is independent of the bending constant (k_{bend}).

3.2. Protein–membrane binding free energy

3.2.1. Continuum potential of mean force calculations

Continuum electrostatics calculations to predict the electrostatic component of the potential of mean force for protein–membrane binding (G^{es}) were carried out in the FEniCS partial differential equation modeling environment [60,61] to solve the Poisson–Boltzmann equations for the mean electrostatic potential appearing in G^{es} (Eq. (3)). The continuum electrostatics calculations make use of membrane and

protein 3D charge and excluded volume profiles via Eq. (4). Bulk electrolyte concentrations were 0.1 M NaCl to mimic experimental conditions. Membrane charge and excluded volume profiles were derived from a 1D fit as described in Appendix A. The profile of the E trimer was taken from the geometry of the experimental structure (PDB 1OK8 [6], Fig. 1c) with waters removed. Fixed charge and volume exclusion profiles for the protein were justified by aligning protein structures from all separations treated in the MD simulations (described below). The alignments showed only a small root mean-square displacement of alpha-carbons among the configurations (RMSD averaged 1.7 Å, see Appendix A).

Each Poisson–Boltzmann calculation used a cubic mesh with 6 tetrahedra per 8 Å³ cube covering the protein- and membrane-occupied regions [62]. Boundary effects were minimized outside this region by adding 24 extra lattice points along each non-periodic direction, with smoothly expanded mesh spacing there to double the box length beyond the central region. The simulation box length was determined from the protein size (or protein plus membrane in the z-direction), plus a 0.5 nm buffer region added on all sides.

Continuum dispersion energy calculations were calculated by numerically integrating the dispersion component of the potential of mean force (G^{disp}, Eq. (5)) on a vertical 1D grid with 0.080 nm spacing.

The continuum and MD potential of mean force (PMF) results were matched by adding a constant energy shift to the MD PMF. No shift in the vertical separation was required since the membrane volume and charge profiles were fit from MD, and the center of mass of the fusion loop (residues 100–109) is unambiguous in both MD and continuum calculations. The magnitude of the shift was determined by overlapping the two curves at a separation of $d = 1$ nm, as shown graphically in Fig. 4c.

3.2.2. All-atom potential of mean force calculations

To estimate the binding free energy between E and the host endosomal membrane, all-atom potential of mean force curves ($W^{aa}(d)$) were computed using Hamiltonian exchange molecular dynamics simulations [53]. The simulations were restrained to a set of 50 protein–membrane separation distances (d) using quadratic biasing potentials centered at 0.3 nm intervals with force constant 1300 kcal/mol/nm², chosen to provide approximately 20% overlap between neighboring biases. The biasing coordinate used was defined as the distance between the center of mass of the alpha carbons on the top 1.5 nm of the protein (away from the membrane) and the lipid headgroups on the far side of the membrane. This indirect approach minimized the chance of structural distortion of the fusion loop and near side of the membrane.

The complete system (Fig. 3a) contained ~339,000 atoms, including ~86,000 waters (TIP3P model), a homogeneously mixed membrane bilayer of 336 and 144 POPC and POPG lipids, respectively, and sodium chloride (at 100 mM ionic strength). Periodic boundary conditions were imposed to avoid surface effects. The hexagonal prism-shaped unit cell (side ~14.5 nm) was generated from the CHARMM-GUI membrane builder and equilibrated for several nanoseconds [63]. This shape maximizes the horizontal separation between the E trimer and its periodic images, which maintained at all times a distance of closest approach greater than ~5.5 nm. Visual inspection of the equilibrated membrane patch showed that it had reached a homogeneous, stable planar bilayer structure. Simulations were run at a temperature of 305 K in the $NP_z\gamma T$ ensemble with interfacial tension $\gamma = 52$ mN/m (necessary for protein insertion and equilibration on an acceptable time scale) using the NAMD2 package [64], with the CHARMM27 force field, CMAP corrections [65], and updates for lipid calculations [66]. Simulations were carried out at 1 bar pressure, with a 1 fs time step, PME electrostatics [67], and 1.2 nm cutoff for non-bonded interactions. During setup, the energy of the 1OK8 E protein trimer structure was minimized and then simulated at 100 K for 100 ps under NVT conditions each for successively smaller harmonic restraints, with energy

constants 250, 100, 50, 10, and 0 kcal/mol/Å². Next, the system was run under production conditions ($NP_z\gamma T$) for 2 ns before pushing the protein into the membrane (1.5 nm over a period of 1.5 ns) to establish 50 initial positions. The coordinate used for pushing was taken as the vertical distance between the center of mass of the alpha carbons on the far 1.5 nm of the protein (away from the membrane, right-most part of protein in Fig. 3a) and the lipid headgroups on the side of the membrane bilayer opposite the fusion loop (membrane/water boundary on the far right of Fig. 3a/b). No orientational constraints were imposed. The pushing coordinate was constrained with a force constant of 2500 kcal/mol/nm² (17.3 N/m), and moved at a rate of 1 nm/ns (1 m/s), which are 10× and 1000× larger and faster than typical values for atomic force microscopy using carbon nanotube probes [68]. The high values used in the simulations are needed to establish initial configurations in a reasonable time. Those values were checked to ensure they do not deform the protein structure (see Appendix A). Paraview and UCSF Chimera [69] were used to prepare Fig. 1.

Hamiltonian exchange simulations were run for 10.5 ns, with the first 5.25 ns considered as equilibration and not used in the final results (Fig. 4). Allowing swapping of neighboring constraints increases the PMF convergence rate by allowing diffusion over constraint space (see Theory for further discussion). The total time for all simulations was 1.05 μs. During the course of the simulation, exchanges between the biasing potentials were attempted every 1 ps with a Metropolis acceptance criteria [55].

Recent protein/surface potential of mean force calculations have used sampling times varying from 4 to 7 ns [53,70], and estimated the drift by computing PMFs for shorter sub-blocks of time. A similar analysis on our PMF data using 10 separate blocks from 5.25 to 10.5 ns shows the estimated PMFs fall within 1 kcal/mol of one another (Fig. 4). Further, there is no noticeable drift in either the PMF or the average trimer separation over the course of the simulation. We conclude that fast motions such as atomic protein–membrane contacts, water hydration and membrane headgroup orientation equilibrate on time scales faster than 0.525 ns, while slow motions such as lateral lipid motion and protein conformational changes are much slower than 5 ns. Therefore the results reported here describe the free energy surface for geometries representing initial protein/membrane contact.

Appendix A provides results on a series of control calculations that establish the soundness of the current approach. First, a detailed analysis of system equilibration and relaxation time scales for the lipid/water interface structure is provided. Next, a plot of protein height and RMSD as a function of distance from the membrane shows that the protein does not change shape during initial pushing or potential of mean force calculations. The membrane response to instantaneous changes in interfacial tension shows that the relaxation time scale of the total membrane surface area is on the order of one nanosecond. Further details are given on fitting protein and membrane volumetric densities for continuum calculations. Finally, Appendix A contains information on the hydration of the fusion loop as a function of membrane distance.

4. Results and discussion

4.1. Membrane bending free energy

To investigate the conditions for which anchoring of E to the endosomal membrane can support fusion, we computed the minimal host membrane bending free energy barrier for formation of the initial fusion stalk (W^{bend}) when the host membrane is contacted by a pentameric face of the virus. The 5-fold sites present the largest open areas on the viral surface. Furthermore, binding to a five-fold face of envelope protein trimers has also been suggested for SFV [71]. The cryo-EM structure of E protein (3IXY) attached to the virus and bound to an antibody specific for the fusion peptide [9] gives an experimental reference geometry. For comparison, we have also carried out the same calculation using the structure of the precursor (pr)-associated E fitted

to a cryo-EM density map (3C6D) [3,4]. These structures from the immature virion exhibit both a non-overlapping packing of E on the viral surface and an outward rotation of E protein's Domain II, which holds the fusion peptide at its tip. The fusion peptide structures in both crystals would be able to contact the host membrane with minimal membrane–membrane separation distance. These two geometries therefore determine a mechanical constraint on the barrier to forming a fusion pore via host membrane bending.

The largest component of the free energy barrier to membrane bending comes from forming a dimple in the host membrane on the opposite side from the virus [33,35,36]. Once formed, the dimple brings the two membranes into contact, and mixing of the outer leaflets is possible with a comparatively smaller energetic barrier [30,32,72]. This suggests that the configuration of the membrane just before stalk formation represents the major free energy barrier. In this configuration, both leaflets of the host endosomal membrane form the dimpled structure (Fig. 1d).

The contact geometry and minimal membrane deformation free energy, W^{bend}, were determined by optimizing the bilayer shape (Fig. 2) under the constraint that the right boundary of the host membrane contacts a specific position of each E protein fusion peptide. That contact position was defined by the alpha carbon of phenylalanine (Phe) 108 E protein cryo-EM structure (PDB ID: 3IXY [9]). The MD results show that this residue sits at the membrane hydrophobic interface on contact with the host. This protein structure, with a partial rotation of Domain II, was used to represent an intermediate between the mature (dimeric) and fusion-active (trimeric) forms of the viral-attached E protein coat [5]. With symmetrical copies of E in the conformation of 3IXY (Fig. 1b), the fusion loops form the vertices of a pentagon with side-length 10.8 nm, at a radius (R_{fus}) of 25.8 nm from the virus center (see Fig. 2a). The distance from the center of the virus particle to E's N-terminal alpha-carbon (R_{term}) is 21.1 nm (see Fig. 1d). Rotating that vector to the center of the pentagon locates the position of the membrane contact at that point, 2.95 nm below the plane of the pentagon of E protein trimers. A similar bending calculation was carried out using the geometry of the 3C6D structure.

Using the elastic surface model described in Section 2 to model the 3C6D geometry results in a lower membrane bending free energy barrier than the simple spherical cap assumed in previous studies [35]. With a membrane monolayer bending modulus of $k_{\text{bend}} = 6.3$ kcal/mol, which experimentally is relatively insensitive to membrane composition [35,73], the free energy of this deformation in the host bilayer is 30 kcal/mol. In comparison, the host membrane bending free energy is 22 kcal/mol for the optimized geometry based on the 3IXY structure (Fig. 1b and d). The intermediate represented by the optimized membrane shape directly precedes the hemifusion state (Fig. 1c), and likely defines the major barrier to membrane fusion. The net curvature is 0.3 nm^{-1} in the center of the dimple at $r = 0$, crosses to negative curvature at $r = 5.8$ nm, and remains near -0.06 nm^{-1} until the assumed contact distance, $R_{\text{bound}} = 9.14$ nm.

The net curvature of 0.3 nm^{-1} at $r = 0$ has a curvature radius similar to the height of a lipid monolayer, which is relatively high [74]. Since the structure of Fig. 2 represents the energetic barrier to fusion, we should expect to find a transition-state structure. It is at this point, in the center of the host membrane dimple, that large stress is required to initiate formation of the fusion stalk. Other elastic models for host membrane deformation find similarly large values at points near the fusion stalk [35,36]. By modeling the deformation using the full parametric-surface elastic theory, the present model shifts a large amount of stress to the point of membrane contact, and consequently finds a free energy comparable to the lowest literature reports for a deformed host membrane structure (e.g., Ref. [36] reported 18–36 kcal/mol from twice the monolayer dimple free energy component, $2F_D$).

The free energy for bending the host endosomal membrane computed here constitutes a major portion of the free energy barrier to stalk formation. Without the aid of membrane proteins, or with passive

membrane-binding proteins, thermal fluctuations of the membrane shape could supply the driving force for overcoming this barrier on the time scale of minutes if the two membranes remained in contact. However, the membranes are unlikely to remain in contact for an appreciable period of time without the aid of fusion proteins [75]. The current mechanism hypothesized for protein-assisted fusion calls for a pH-driven conformational change of E to allow host membrane attachment and drive the fusion event. That mechanism is supported by a rotation of Domain II relative to the base Domains I and III between structures of pre- and post-fusion E conformations [5].

The 50-residue C-terminal stem region of E, omitted in this study due to lack of a crystal structure, connects Domain III with two alpha-helices anchoring the protein to the viral membrane [76]. Binding of the stem along Domain II results in colocation of the anchor region and the host membrane-inserted fusion loop (Fig. 1c) [77]. Although the alpha helical anchor regions must completely traverse the viral membrane to be effective aids to fusion [78], E's fusion loop merely binds to the outer leaflet of the host. This shallow insertion may suggest that the fusion loop acts to nucleate a curvature-defect to disrupt the stability of the outer host leaflet and promote fusion with the viral membrane. Curvature defect mechanisms have been suggested in several experimental models of proteins promoting and inhibiting membrane fusion [79–81].

4.2. Protein–membrane binding free energy

The geometry of the protein–membrane–water atomistic systems can be seen from plots of water density (Fig. 3b). Although the z-center is often defined as the bilayer center, we define the zero in the membrane normal direction as the average location of the glycerol carbons of the bilayer surface that contacts the protein. The density was calculated as conditional averages over water histograms (Eq. (6)), defined in one dimension along the z-coordinate. Using the average height of the membrane's glycerol carbon atoms to define the origin of the horizontal axis (membrane normal direction), the region of zero water density at either side of the plot ($z \sim 1$ or ~ 12 nm) shows the hydrophobic width of the membrane. The system is wrapped so that half of the membrane appears on the far right (Fig. 3a).

The region of bulk water density (maroon color, outlined by white contours) shows that at the largest protein–membrane separations (top of Fig. 3b), the protein is adequately separated from both membrane/water interfaces. Continuum calculations also verified negligible interaction at this distance. The geometrical center of the protein's fusion loop (residues 100–108) appears on the left side of the plot, indicated by a black line. The bulk water density region is outlined by white contour lines at 1 and 54 mol/L. Fig. 3a shows a protein configuration chosen at random from samples at 0.0 nm distance. The far end of the protein has a larger diameter, as shown by the slightly smaller water density (Fig. 3b) at a distance of 10 nm from the membrane surface. This end would normally be linked by the C-terminal stem to the viral membrane surface. Here the protein is modeled as free in solution, as in experiments involving truncated soluble E (sE) protein [82].

Despite incursion of the protein into the membrane, the membrane interface density profile shows little variation with protein–membrane separation distance and only a small amount of water is carried into the membrane by the fusion loop (Fig. 3b). This simplifies modeling of the membrane interface since water density profiles can be obtained by averaging over all separations (see Appendix A).

The membrane shape, interfacial tension and hydrophobic thickness are important determinants of the binding and electrostatic properties of the membrane/water interface [83]. Both membrane–water interfaces, defined using the water density profile normal to the membrane, fit well to an error-function,

$$\kappa_m(z) = \frac{1}{2}(\mathrm{erf}(w(z - z_0 + D_c)) - \mathrm{erf}(w(z - z_0 - D_c))). \qquad (7)$$

The membrane fit to $w = 1.58$ nm^{-1}, $2D_c = 2.899$ nm, and centered at $z_0 = 1.261$ nm with respect to the average glycerol carbon position. The parameter w indicates the interfacial roughness.

Defining the water/membrane dividing surface as the position where water reaches half its bulk density, the hydrophobic width for half the bilayer is given here by the parameter, D_c. The hydrophobic width of 2.9 nm for the full bilayer compares well with experimental measurements of 2.87 nm for pure POPE [84], and 2.71 nm for pure POPC [85]. The layer of glycerol carbons lies just inside the hydrophobic interface, confirming that water fully hydrates the lipid head-groups. Redefining the dividing surface as the mean position of the glycerol carbon layer ($d = 0$ of Fig. 4) to compare better with experimental analysis would decrease the estimate of the hydrophobic width by $2(D_c - z_0) \sim 0.4$ nm. The dispersion coefficient densities (used in Eq. (5)) for protein and membrane fit to a linear model with a residual of around 0.5%. More details are available in Appendix A.

Because the process of membrane insertion may change the interfacial area, constant interfacial tension conditions are required. Finite size effects have been reported for simulation of small membranes (18 lipid molecules) using the NPγT ensemble [86]. These effects have been attributed to the inability of smaller simulations to describe capillary waves. However, a more recent comparison of simulation sizes containing 72 and 288 DOPC lipids (1,2-dioleoyl-sn-glycero-3-phosphocholine) [87] have shown that finite size effects are negligible for these larger system sizes. This conclusion agrees with thorough studies of the relationship between surface tension and capillary waves at the water/vapor interface [88], which showed a small, but statistically insignificant increase in tension with simulation area. With 480 lipids in the unit cell with side-length 14.5 nm, the present results should also be expected to exhibit negligible finite size effects.

4.2.1. Combined potential of mean force

The protein–membrane binding free energy profiles computed using both continuum and atomistic methods are shown in Fig. 4, along with the membrane and solvent charge density to identify the membrane bilayer structure. Establishing an absolute scale for the binding free energy from MD requires consideration of both the absolute shift in the free energy and possible artifacts from the periodicity of the MD system. Periodicity artifacts were ruled out by carrying out continuum calculations (Eq. (3)) with a periodic boundary in the z-direction. Both dispersion and electrostatic energy components were identical to their periodic versions at protein–membrane separations closer than 1.3 nm. At separations larger than 2 nm, both continuum components approached zero. Since the MD simulation did not explore separations larger than 1.3 nm, the error from periodic boundary conditions in MD is negligible. Alignment of continuum and MD results at a large separation of $d = 1$ nm (Fig. 4) identifies the zero for the MD free energy profiles with a precision of 0.23 kcal/mol. This constant shift in W^{aa} sets an absolute energy scale that is not identifiable from the MD data alone.

At separations greater than 1 nm, most of the binding free energy can be predicted using the continuum model. At closer separations, encroachment of the protein causes the fluid membrane to rearrange locally, resulting in specific chemical interactions between the protein and membrane. This packing free energy and replacement of protein–water hydrogen-bonds by protein interactions with lipid headgroups accounts for the difference between the continuum and molecular models. Fig. 4 shows this free energy difference is positive since the MD curve, W^{aa}, lies above the continuum curve, $G^{es} + G^{disp}$. While the continuum calculation predicts a favorable binding free energy, packing and chemical interactions accounted for in the MD simulations make binding significantly less favorable. Unfavorable repulsive contacts accounted for in the MD simulations also flatten and shift the minimum predicted by the continuum model outward by 0.5 nm so that the E protein trimer inserts at a depth of 0.13 nm into the hydrophobic core of the PC/PG bilayer.

We note that the magnitude of the hydrophobic effect may be underestimated due to infidelities in the force field model. This inaccuracy was reported in other MD calculations of protein-surface potential of mean force curves using the same force field, where it was attributed to an overly strong attraction of water by the surface [70]. Underestimating the magnitude of the hydrophobic effect would result in a binding free energy (our stated value of − 15 kcal/mol) that is less favorable than the actual value.

4.2.2. Bound protein structure

We observe two changes as the fusion peptide inserts into the hydrophobic portion of the membrane. First, hydrophobic residues on the fusion loop "open" into a vertical orientation of the aromatic rings. A similar opening was reported in NMR studies [24]. Just outside the membrane surface, the hydrophobic residues close to a horizontal orientation, presumably to minimize contact area of the trimer center with water. Second, along with this opening motion, we note that the trimer interface begins to expand at the tip with E insertion. The expansion means the trimer interface holds together less effectively.

To quantify the expansion, we plot the area of the triangle formed by the inward-facing carbonyl oxygens of the E trimer's Phe108 residues as the fusion loop approaches the membrane (Fig. 5). The plot was calculated using conditional averages of histogram densities with Eq. (6). At contact with the mixed neutral and anionic (7:3 POPC/POPG) membrane, the area doubles from its value of $0.16 \, nm^2$ observed in the trimer crystal structure (1OK8) [6]. An even larger expansion was observed in MD simulations of the trimer in bulk solution [89]. The appearance of the more open conformation could indicate that the E trimer inserts in the open form, or that E inserts as monomers rather than a trimer. All available structures for the E protein trimer were obtained in the absence of a lipid membrane. The detailed structure of the membrane-inserted trimer is unknown apart from NMR and MD studies on the fusion peptide fragment [24,25].

Experimental evidence suggests that a C-terminal fragment of the protein (not modeled here) zips along the protein to close the trimer interface during the fusion process [77]. During the zipping process, the strong protein–membrane binding energy keeps E's fusion loop in contact with the host. This is consistent with experimental data indicating that fusion occurs readily for the 30% anionic PG composition

studied here [29,27]. A closing motion of the E trimer may alter the membrane shape toward the negative curvature required by the fusion stalk (Figs. 1–2).

The flexibility of the Domain II hinge also suggests another possible mechanism for sensitivity to the host membrane's lipid composition. If the cluster of positively-charged arginine residues just above the fusion loop gathers anionic lipids together around its outward edge, that lipid rearrangement may compress the area normally taken up by the anionic headgroups. This change in area would create a preference for negative curvature in the host membrane at that site that favors fusion (Fig. 1b–c). In this case, lipids that are both anionic and have positive intrinsic curvature would resist E-assisted fusion. The effect of protein binding and insertion on membrane curvature awaits experimental testing. Such a lipid rearrangement would occur on a longer time scale than was simulated in the present study.

5. Conclusions

Both atomistic and continuum models present a consistent energetic picture of virus-assisted membrane fusion (Fig. 4). Our results quantify the initial binding strength between each E protein trimer and host membranes enriched with anionic lipids. The insertion depth predicted here can be experimentally confirmed using neutron reflectivity experiments [90]. The binding free energy predicted here can be compared with experimental values for peptides determined by quantifying membrane-associated fractions [41,91].

At large separations (> 1 nm), both electrostatic and dispersion interactions help pull E toward mixed neutral and anionic PC/PG membranes. At contact distance, molecular packing and association interactions fully counter the favorable electrostatic attraction, halting the fusion peptide 0.13 nm into the hydrophobic core of the PC/PG membrane. Combining continuum calculations with an all-atom potential of mean force results in a binding free energy of − 15 kcal/mol per trimer. The atomistic potential of mean force computed after 10 ns of simulation time represents the free energy of a relatively stable intermediate bound state. Large-scale structural changes due to membrane relaxation occurring on longer time scales may further strengthen the protein/membrane association free energy. Thus, the binding free energy predicted here represents an upper bound.
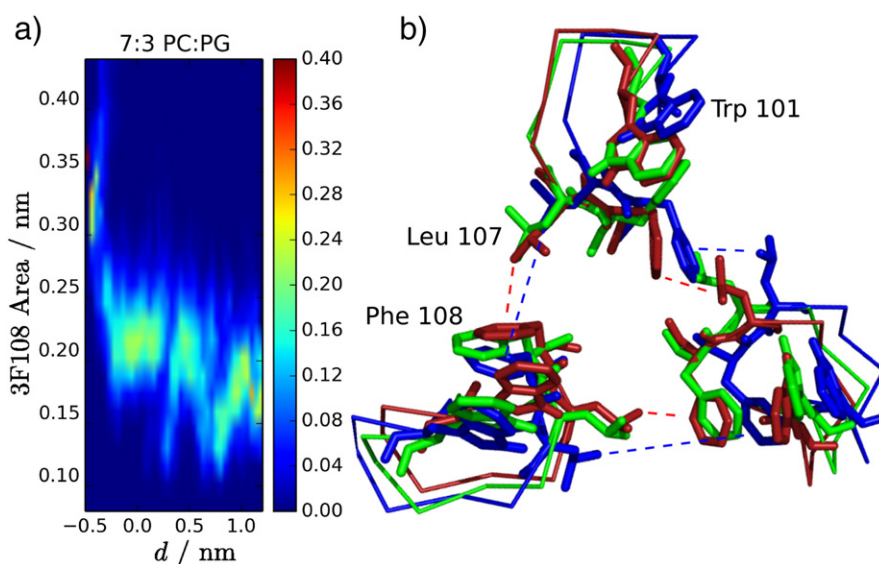
Fig. 5. (a) Probability distribution (colored scale on right) computed for the area of the triangle between the three Phe108 (also notated F108) carbonyl oxygen atoms of E protein trimer as a function of membrane to fusion loop separation distance, d. Length is given in nm units. (b) Superposition of fusion loop backbone trace and all heavy atoms of Trp101, Leu107, and Phe108, viewed from the membrane. The 3 configurations shown are colored in order of decreasing distance to the membrane in the sequence red, green, blue. Lines highlight the increasing distance between Leu107 and Phe108 from alternate subunits.

When the host membrane is contacted simultaneously by 5 E trimers from the viral surface, the total association free energy is at least as strong as − 75 kcal/mol. This is overwhelmingly larger than the free energy barrier for membrane fusion, which we estimate to be 22–30 kcal/mol. For the latter prediction, we used an elastic bending model constrained by the geometries of the cryo-EM structures for viral complexes 3C6D and 3IXY. That value is consistent with the dimple formation free energies derived in recent calculations of the fusion stalk structure, which range from 18 to 36 kcal/mol [36]. A free energy barrier of 20 kcal/mol is sufficiently small to allow unassisted fusion over an O(10 s) time scale, but only if the membranes are held in contact for that long time period.

The free energy of the overall fusion process will be influenced strongly by host membrane curvature. Elastic calculations show that asymmetric membranes favoring positive curvature [79] reduce the energy barrier for host dimple formation to around 3–21 kcal/mol [34,33]. Long-wavelength membrane undulations will also effectively increase the available thermal energy. The driving force of a protein conformational change has to be interpreted with these considerations in mind [81].

This study presents a novel pathway to computing the free energies of membrane-associated processes. Future large-scale modeling of protein–membrane and membrane–membrane interactions would be improved by including membrane excluded volume and charge profiles from all-atom simulations. Detailed atomistic calculation of interfacial behavior is critical in those continuum descriptions [92,93]. In similarity with most colloidal systems, the protein–membrane interactions include weak long-range dispersive attractions, whose importance increases with electrolyte concentration [50], as well as electrostatic and short-ranged interactions. When combined with traditional membrane curvature calculations as in Section 2.1, the model can be applied to phenomena at biological length- and time-scales. Tying advances in molecular models with continuum predictions requires robust, extensible simulation codes at both levels of description. Important developments continue to be made in electrostatics [61,94,95], high-fidelity boundary-element methods [96,97], and models [34,73,98] for inter- and intra-membrane interactions that will facilitate comparison with experimental reference data [49,51,84,99,100]. Such developments will be key to developing this model further to enable rapid prediction of the effect of chemical environment on the process of viral protein-assisted membrane fusion.

Particularly important future targets for these models include extending the binding free energy calculations to different membrane compositions to identify the minimum percentage of anionic lipid needed to prevent detachment of E from the host membrane. Similar calculations for cholesterol-containing membranes will establish the relative anchoring free energies provided by cholesterol compared with anionic lipids. At close separation, there is an energetic trade-off between the protein's conformation and its attraction to the membrane vs. the host membrane bending needed to initiate fusion. The protein–membrane binding free energies in alternative protein positions, such as the side-on interaction during initial protein–membrane recognition suggested by the alignment of Fig. 1b, and membrane–membrane interaction are also open targets for future work.

Acknowledgement

Appendix A. Supplementary data

Supplementary data to this article can be found online at http://dx.doi.org/10.1016/j.bbamem.2014.12.018.

References

[1] World Health Organization, Dengue and severe dengue, WHO Fact Sheet, 1172012.
[2] Y. Zhang, Structures of immature flavivirus particles, EMBO J. 22 (11) (2003) 2604–2613.
[3] Ying Zhang, Wei Zhang, Steven Ogata, David Clements, James H. Strauss, Timothy S. Baker, Richard J. Kuhn, Michael G. Rossmann, Conformational changes of the flavivirus e glycoprotein, Structure 12 (9) (2004) 1607–1618.
[4] L. Li, S.-M. Lok, I.-M. Yu, Y. Zhang, R.J. Kuhn, J. Chen, M.G. Rossmann, The flavivirus precursor membrane-envelope protein complex: structure and maturation, Science 319 (5871) (2008) 1830–1834.
[5] Xiaokang Zhang, Peng Ge, Xuekui Yu, Jennifer M. Brannan, Guoqiang Bi, Qinfen Zhang, Stan Schein, Z. Hong Zhou, Cryo-EM structure of the mature dengue virus at 3.5-Å resolution, Nat. Struct. Mol. Biol. 20 (2013) 105–110.
[6] Yorgo Modis, Steven Ogata, David Clements, Stephen C. Harrison, Structure of the dengue virus envelope protein after membrane fusion, Nature 427 (6972) (2004) 313–319.
[7] Elena Pokidysheva, Ying Zhang, Anthony J. Battisti, Carol M. Bator-Kelly, Paul R. Chipman, Chuan Xiao, G. Glenn Gregorio, Wayne A. Hendrickson, Richard J. Kuhn, Michael G. Rossmann, Cryo-EM reconstruction of dengue virus in complex with the carbohydrate recognition domain of DC-SIGN, Cell 124 (3) (February 2006) 485–493.
[8] Shee-Mei Lok, Victor Kostyuchenko, Grant E. Nybakken, Heather A. Holdaway, Anthony J. Battisti, Soila Sukupolvi-Petty, Dagmar Sedlak, Daved H. Fremont, Paul R. Chipman, John T. Roehrig, Michael S. Diamond, Richard J. Kuhn, Michael G. Rossmann, Binding of a neutralizing antibody to dengue virus alters the arrangement of surface glycoproteins, Nat. Struct. Mol. Biol. 15 (3) (2008) 312–317.
[9] Mickaël V. Cherrier, Brbel Kaufmann, Grant E. Nybakken, Shee-Mei Lok, Julia T. Warren, Beverly R. Chen, Christopher A. Nelson, Victor A. Kostyuchenko, Heather A. Holdaway, Paul R. Chipman, Richard J. Kuhn, Michael S. Diamond, Michael G. Rossmann, Daved H. Fremont, Structural basis for the preferential recognition of immature flaviviruses by a fusion-loop antibody, EMBO J. 28 (20) (2009) 3269–3276.
[10] Erika Navarro-Sanchez, Ralf Altmeyer, Ali Amara, Olivier Schwartz, Franck Fieschi, Jean-Louis Virelizier, Fernando Arenzana-Seisdedos, Philippe Desprès, Dendritic-cell-specific ICAM3-grabbing non-integrin is essential for the productive infection of human dendritic cells by mosquito-cell-derived dengue viruses, EMBO Rep. 4 (7) (2003) 723–728.
[11] Boonrat Tassaneetrithep, Timothy H. Burgess, Angela Granelli-Piperno, Christine Trumpfheller, Jennifer Finke, Wellington Sun, Michael A. Eller, Kovit Pattanapanyasat, Suttipant Sarasombath, Deborah L. Birx, Ralph M. Steinman, Sarah Schlesinger, Mary A. Marovich, DC-SIGN (CD209) mediates dengue virus infection of human dendritic cells, J. Exp. Med. 197 (7) (2003) 823–829.
[12] Y. Modis, S. Ogata, D. Clements, S.C. Harrison, Variable surface epitopes in the crystal structure of dengue virus type 3 envelope glycoprotein, J. Virol. 79 (2) (2005) 1223–1231.
[13] Yaping Chen, Terry Maguire, Ronald E. Hileman, Jonathan R. Fromm, Jeffrey D. Esko, Robert J. Linhardt, Rory M. Marks, Dengue virus infectivity depends on envelope protein binding to target cell heparan sulfate, Nat. Med. 3 (8) (1997) 866–871.
[14] Nadine Dalrymple, Erich R. Mackow, Productive dengue virus infection of human endothelial cells is directed by heparan sulfate-containing proteoglycan receptors, J. Virol. 85 (18) (2011) 9478–9485.
[15] Karin Stiasny, Franz X. Heinz, Flavivirus membrane fusion, J. Gen. Virol. 87 (10) (2006) 2755–2766.
[16] Stephen C. Harrison, Viral membrane fusion, Nat. Struct. Mol. Biol. 15 (2008) 690–698.
[17] Jeroen Corver, Antonio Ortiz, Steven L. Allison, Juliane Schalich, Franz X. Heinz, Jan Wilschut, Membrane fusion activity of tick-borne encephalitis virus and recombinant subviral particles in a liposomal model system, J. Virol. 269 (1) (2000) 37–46.
[18] Karin Stiasny, Christian Koessl, Franz X. Heinz, Involvement of lipids in different steps of the flavivirus fusion mechanism, J. Virol. 77 (14) (2003) 7856–7862.
[19] S.W. Gollins, J.S. Porterfield, pH-dependent fusion between the flavivirus West Nile and liposomal model membranes, J. Gen. Virol. 67 (1986) 157–166.
[20] T. Phalen, M. Kielian, Cholesterol is required for infection by semliki forest virus, J. Cell Biol. 112 (4) (1991) 615–623.
[21] M. Umashankar, Claudia Sánchez-San Martín, Maofu Liao, Brigid Reilly, Alice Guo, Gwen Taylor, Margaret Kielian, Differential cholesterol binding by class II fusion proteins determines membrane fusion properties, J. Virol. 82 (18) (2008) 9245–9253.
[22] Elena Zaitseva, Sung-Tae Yang, Kamran Melikov, Sergei Pourmal, Leonid V. Chernomordik, Dengue virus ensures its fusion in late endosomes using compartment-specific lipids, PLoS Pathog. 6 (10) (2010) e1001131.
[23] J. Justman, M.R. Klimjack, M. Kielian, Role of spike protein conformational changes in fusion of semliki forest virus, J. Virol. 67 (12) (1993) 7597–7607.
[24] Manuel Nuno Melo, Francisco J.R. Sousa, Fabiana A. Carneiro, Miguel A.R.B. Castanho, Ana Paula Valente, Fabio C.L. Almeida, Andrea T. Da Poian, Ronaldo Mohana-Borges, Interaction of the dengue virus fusion peptide with membranes

assessed by NMR: the essential role of the envelope protein Trp101 for membrane fusion, J. Mol. Biol. 392 (2009) 736–746.

[25] Jinhe Pan, C. Benjamin Lai, Walter R.P. Scott, Suzana K. Straus, Synthetic fusion peptides of tick-borne encephalitis virus as models for membrane fusion, Biochemistry 49 (2) (2010) 287–296.

[26] Elizabeth A. Christian, Kristen M. Kahle, Kimberly Mattia, Bridget A. Puffer, Jennifer M. Pfaff, Adam Miller, Cheryl Paes, Edgar Davidson, Benjamin J. Doranz, Atomic-level functional model of dengue virus envelope protein infectivity, Proc. Natl. Acad. Sci. U. S. A. 110 (46) (2013) 18662–18667.

[27] Leonid V. Chernomordik, Michael M. Kozlov, Mechanics of membrane fusion, Nat. Struct. Mol. Biol. 15 (7) (2008) 675–683.

[28] Leonid Chernomordik, Alexandr Chanturiya, Julie Green, Joshua Zimmerberg, The hemifusion intermediate and its conversion to complete fusion: regulation by membrane composition, Biophys. J. 69 (1995) 922–929.

[29] L. Chernomordik, M.M. Kozlov, J. Zimmerberg, Lipids in biological membrane fusion, J. Membr. Biol. 146 (1) (1995) 1–14.

[30] Dina Mirjanian, Allison N. Dickey, Jan H. Hoh, Thomas B. Woolf, Mark J. Stevens, Splaying of aliphatic tails plays a central role in barrier crossing during liposome fusion, J. Phys. Chem. B 114 (34) (2010) 11061–11068.

[31] Peter M. Kasson, Vijay S. Pande, Control of membrane fusion mechanism by lipid composition: predictions from ensemble molecular dynamics, PLoS Comput. Biol. 3 (11) (2007) e220.

[32] Mark J. Stevens, Jan H. Hoh, Thomas B. Woolf, Insights into the molecular mechanism of membrane fusion from simulation: evidence for the association of splayed tails, Phys. Rev. Lett. 91 (Oct 2003) 188102.

[33] Yonathan Kozlovsky, Michael M. Kozlov, Stalk model of membrane fusion: solution of energy crisis, Biophys. J. 82 (2) (2002) 882–895.

[34] Peter I. Kuzmin, Joshua Zimmerberg, Yuri A. Chizmadzhev, Fredric S. Cohen, A quantitative model for membrane fusion based on low-energy intermediates, Proc. Natl. Acad. Sci. U. S. A. 98 (13) (2001) 7235–7240.

[35] V.S. Markin, J.P. Albanesi, Membrane fusion: stalk model revisited, Biophys. J. 82 (2002) 693–712.

[36] Sylvio May, Structure and energy of fusion stalks: the role of membrane edges, Biophys. J. 83 (6) (2002) 2969–2980.

[37] A. Jain, H.S. Ashbaugh, Digging a hole: scaled-particle theory and cavity solvation in organic solvents, J. Chem. Phys. 129 (17) (2008) 174505.

[38] S. Hyde, Z. Blum, T. Landh, S. Lidin, B.W. Ninham, S. Andersson, K. Larsson, The Language of Shape: The Role of Curvature in Condensed Matter, Elsevier, 1996.

[39] Stéphane Bressanelli, Karin Stiasny, Steven L. Allison, Enrico A. Stura, Stéphane Duquerroy, Julien Lescar, Franz X. Heinz, Félix A. Rey, Structure of a flavivirus envelope glycoprotein in its low-pH-induced membrane fusion conformation, EMBO J. 23 (2004) 728–738.

[40] Bärbel Kaufmann, Paul R. Chipman, Heather A. Holdaway, Syd Johnson, Daved H. Fremont, Richard J. Kuhn, Michael S. Diamond, Michael G. Rossmann, Capturing a flavivirus pre-fusion intermediate, PLoS Pathog. 5 (11) (2009) e1000672.

[41] N. Ben-Tal, B. Honig, C. Miller, S. McLaughlin, Electrostatic binding of proteins to membranes. Theoretical predictions and experimental results with charybdotoxin and phospholipid vesicles, Biophys. J. 73 (4) (1997) 1717–1727.

[42] Andrei L. Lomize, Irina Pogozheva, Henry I. Mosberg, Anisotropic solvent model of the lipid bilayer. 2. Energetics of insertion of small molecules, peptides and proteins in membranes, J. Chem. Inf. Model. 51 (4) (2011) 930–946.

[43] Luca Monticelli, Senthil K. Kandasamy, Xavier Periole, Ronald G. Larson, D. Peter Tieleman, Siewert-Jan Marrink, The MARTINI coarse-grained force field: extension to proteins, J. Chem. Theory Comput. 4 (5) (2008) 819834.

[44] Zhe Wu, Qiang Cui, Arun Yethiraj, A new coarse-grained force field for membrane peptide simulations, J. Chem. Theory Comput. 7 (11) (2011) 3793–3802.

[45] See-Wing Chiu, Sagar A. Pandit, H.L. Scott, Eric Jakobsson, An improved united atom force field for simulation of mixed lipid bilayers, J. Phys. Chem. B 113 (9) (2009) 2748–2763.

[46] Robert A. Latour, Molecular simulation of protein–surface interactions: benefits, problems, solutions, and future directions, Biointerphases 3 (3) (2008) FC2–FC12.

[47] C.P. O'Brien, S.J. Stuart, D.A. Bruce, R.A. Latour, Modeling of peptide adsorption interactions with a poly(lactic acid) surface, Langmuir 24 (24) (2008) 14115–14124.

[48] Keith M. Callenberg, Om P. Choudhary, Gabriel L. de Forest, David W. Gohara, Nathan A. Baker, Michael Grabe, APBSmem: a graphical interface for electrostatic calculations at the membrane, PLoS One 5 (9) (09 2010) e12722.

[49] S. Leikin, V.A. Parsegian, D.C. Rau, R.P. Rand, Hydration forces, Annu. Rev. Phys. Chem. 44 (1993) 369–395.

[50] Drew F. Parsons, Mathias Boström, Pierandrea Lo Nostro, Barry W. Ninham, Hofmeister effects: interplay of hydration, nonelectrostatic potentials, and ion size, Phys. Chem. Chem. Phys. 13 (2011) 12352–12367.

[51] Horia I. Petrache, Thomas Zemb, Luc Belloni, V. Adrian Parsegian, Salt screening and specific ion adsorption determine neutral-lipid membrane interactions, Proc. Natl. Acad. Sci. U. S. A. 103 (21) (2006) 7982–7987.

[52] David M. Rogers, Dian Jiao, Lawrence R. Pratt, Susan B. Rempe, Structural models and molecular thermodynamics of hydration of ions and small molecules, in: R. Wheeler (Ed.), Annu. Rep. Comput. Chem., vol. 8, Elsevier, 2012, pp. 71–127.

[53] Libo Li, Igor Vorobyov, Toby W. Allen, Potential of mean force and pKa profile calculation for a lipid membrane-exposed arginine side chain, J. Phys. Chem. B 112 (32) (2008) 9574–9587.

[54] Chris Neale, Tomas Rodinger, Régis Pomès, Equilibrium exchange enhances the convergence rate of umbrella sampling, Chem. Phys. Lett. 460 (1–3) (2008) 375–381.

[55] John D. Chodera, Michael R. Shirts, Replica exchange and expanded ensemble simulations as Gibbs sampling: simple improvements for enhanced mixing, J. Chem. Phys. 135 (19) (2011) 194110.

[56] Michael R. Shirts, John D. Chodera, Statistically optimal analysis of samples from multiple equilibrium states, J. Chem. Phys. 129 (12) (2008) 124105.

[57] L.R. Pratt, S.B. Rempe, Quasi-chemical theory and implicit solvent models for simulations, in: G. Hummer, L.R. Pratt (Eds.), Simulation and theory of electrostatic interactions in solution, AIP Conference Proceedings, vol. 492, AIP Press, New York, 1999, pp. 172–201.

[58] T.L. Beck, M.E. Paulaitis, L.R. Pratt, The Potential Distribution Theorem and Models of Molecular Solutions, 2006. (Cambridge, New York).

[59] D. Asthagiri, P.D. Dixit, S. Merchant, M.E. Paulaitis, L.R. Pratt, Susan B. Rempe, Sameer Varma, Ion selectivity from local configurations of ligands in solutions and ion channels, Chem. Phys. Lett. 485 (2010) 1–7.

[60] A. Logg, G.N. Wells, Dolfin: automated finite element computing, ACM Trans. Math. Softw. 32 (2) (2010) 1–28.

[61] Anders Logg, Kent-Andre Mardal, Garth Wells (Eds.), Automated Solution of Differential Equations by the Finite Element Method, Springer, 2012.

[62] A. Logg, Efficient representation of computational meshes, Int. J. Comput. Sci. Eng. 4 (4) (2009) 283–295.

[63] Sunhwan Jo, Joseph B. Lim, Jeffery B. Klauda, Wonpil Im, CHARMM-GUI membrane builder for mixed bilayers and its application to yeast membranes, Biophys. J. 97 (1) (2009) 50–58.

[64] Laxmikant Kalé, Robert Skeel, Milind Bhandarkar, Robert Brunner, Attila Gursoy, Neal Krawetz, James Phillips, Aritomo Shinozaki, Krishnan Varadarajan, Klaus Schulten, NAMD2: greater scalability for parallel molecular dynamics, J. Comput. Phys. 151 (1) (1999) 283–312.

[65] A.D. MacKerell, D. Bashford, R.L. Dunbrack Bellott, J.D. Evanseck, M.J. Field, S. Fischer, J. Gao, H. Guo, S. Ha, D. Joseph-McCarthy, L. Kuchnir, K. Kuczera, F.T.K. Lau, C. Mattos, S. Michnick, T. Ngo, D.T. Nguyen, B. Prodhom, W.E. Reiher, B. Roux, M. Schlenkrich, J.C. Smith, R. Stote, J. Straub, M. Watanabe, J. Wirkiewicz-Kuczera, D. Yin, M. Karplus, All-atom empirical potential for molecular modeling and dynamics studies of proteins, J. Phys. Chem. B 102 (18) (1998) 3586–3616.

[66] Jeffery B. Klauda, Richard M. Venable, J. Alfredo Freites, Joseph W. OConnor, Douglas J. Tobias, Carlos Mondragon-Ramirez, Igor Vorobyov, Alexander D. MacKerell Jr., Richard W. Pastor, Update of the CHARMM all-atom additive force field for lipids: validation on six lipid types, J. Phys. Chem. B 114 (2010) 7830–7843.

[67] U. Essmann, L. Perera, M.L. Berkowitz, T. Darden, H. Lee, L.G. Pedersen, A smooth particle mesh Ewald method, J. Chem. Phys. 103 (1995) 8577–8592.

[68] Liwei Chen, Chin Li Cheung, Paul D. Ashby, Charles M. Lieber, Single-walled carbon nanotube AFM probes: optimal imaging resolution of nanoclusters and biomolecules in ambient and fluid environments, Nano Lett. 4 (9) (2004) 1725–1731.

[69] E.F. Pettersen, T.D. Goddard, C.C. Huang, G.S. Couch, D.M. Greenblatt, E.C. Meng, T.E. Ferrin, UCSF chimera — a visualization system for exploratory research and analysis, J. Comput. Chem. 25 (13) (2004) 1605–1612.

[70] Nadeem A. Vellore, Jeremy A. Yancey, Galen Collier, Robert A. Latour, Steven J. Stuart, Assessment of the transferability of a protein force field for the simulation of peptide–surface interactions, Langmuir 26 (10) (2010) 7396–7404.

[71] Don L. Gibbons, Marie-Christine Vaney, Alain Roussel, Armelle Vigouroux, Brigid Reilly, Jean Lepault, Margaret Kielian, Félix A. Rey, Conformational change and protein–protein interactions of the fusion protein of Semliki Forest virus, Nature 427 (2004) 320–325.

[72] Peter M. Kasson, Erik Lindahl, Vijay S. Pande, Water ordering at membrane interfaces controls fusion dynamics, J. Am. Chem. Soc. 133 (11) (2011) 3812–3815.

[73] Grace Brannigan, Frank L.H. Brown, A consistent model for thermal fluctuations and protein-induced deformations in lipid bilayers, Biophys. J. 90 (5) (2006) 1501–1520.

[74] R.P. Rand, V.A. Parsegian, Hydration, curvature, and bending elasticity of phospholipid monolayers, Curr. Top. Membr. 44 (1998) 167–189. (This work reverses the sign of radii of curvature relative to the present convention. For example, the work's results state DOPE prefers to form inverted hexagonal phases around water-filled cylinders with $R_0 = 2.85$ nm.)

[75] Ilya Plonsky, David H. Kingsley, Afshin Rashtian, Paul S. Blank, Joshua Zimmerberg, Initial size and dynamics of viral fusion pores are a function of the fusion protein mediating membrane fusion, Biol. Cell. 100 (2008) 377–386.

[76] Su-Ru Lin, Gang Zou, Szu-Chia Hsieh, Min Qing, Wen-Yang Tsai, Pei-Yong Shi, Wei-Kung Wang, The helical domains of the stem region of dengue virus envelope protein are involved in both virus assembly and entry, J. Virol. 85 (10) (2011) 5159–5171.

[77] Daryl E. Klein, Jason L. Choi, Stephen C. Harrison, Structure of a dengue virus envelope protein late-stage fusion intermediate, J. Virol. 87 (4) (2013) 2287–2293.

[78] R. Todd Armstrong, Anna S. Kushnir, Judith M. White, The transmembrane domain of influenza hemagglutinin exhibits a stringent length requirement to support the hemifusion to fusion transition, J. Cell Biol. 151 (2) (2000) 425–437.

[79] Leonid V. Chernomordik, Eugenia Leikina, Vadim Frolov, Peter Bronk, Joshua Zimmerberg, An early stage of membrane fusion mediated by the low ph conformation of influenza hemagglutinin depends upon membrane lipids, J. Cell Biol. 136 (1) (1997) 81–93.

[80] Karin Stiasny, Franz X. Heinz, Effect of membrane curvature-modifying lipids on membrane fusion by tick-borne encephalitis virus, J. Virol. 78 (16) (2004) 8536–8542.

[81] Kun Li, Ruben M. Markosyan, Yi-Min Zheng, Ottavia Golfetto, Brittani Bungart, Minghua Li, Shilei Ding, Yuxian He, Chen Liang, James C. Lee, Enrico Gratton, Fredric S. Cohen, Shan-Lu Liu, IFITM proteins restrict viral membrane hemifusion, PLoS Pathog. 9 (1) (2013) e1003124.

[82] Aihua Zheng, Mahadevaiah Umashankar, Margaret Kielian, In vitro and in vivo studies identify important features of dengue virus pr-e protein interactions, PLoS Pathog. 6 (10) (2010) e1001157.

[83] Ryan W. Benz, Francisco Castro-Román, Douglas J. Tobias, Stephen H. White, Experimental validation of molecular dynamics simulations of lipid bilayers: a new approach, Biophys. J. 88 (2) (2005) 805–817.

[84] L.J. Lis, M. McAlister, N. Fuller, R.P. Rand, V.A. Parsegian, Interactions between neutral phospholipid bilayer membranes, Biophys. J. 37 (3) (1982) 657–665.

[85] Norbert Kučerka, Stephanie Tristram-Nagle, John F. Nagle, Structure of fully hydrated fluid phase lipid bilayers with monounsaturated chains, J. Membr. Biol. 208 (2005) 193–202.

[86] S.E. Feller, R.W. Pastor, On simulating lipid bilayers with an applied surface tension: periodic boundary conditions and undulations, Biophys. J. 71 (3) (1996) 1350–1355.

[87] F. Castro-Román, R.W. Benz, S.H. White, D.J. Tobias, Investigation of finite system-size effects in molecular dynamics simulations of lipid bilayers, J. Phys. Chem. B 110 (47) (2006) 24157–24164.

[88] Ahmed E. Ismail, Gary S. Grest, Mark J. Stevens, Capillary waves at the liquid–vapor interface and the surface tension of water, J. Chem. Phys. 125 (1) (2006).

[89] Kshatresh Dutta Dubey, Amit Kumar Chaubey, Rajendra Prasad Ojha, Stability of trimeric DENV envelope protein at low and neutral pH: an insight from MD study, Biochim. Biophys. Acta Protein Proteomics 1834 (1) (2013) 53–64.

[90] D.J. McGillivray, G. Valincius, F. Heinrich, J.W.F. Robertson, D.J. Vanderah, W. Febo-Ayala, I. Ignatjev, M. Losche, J.J. Kasianowicz, Structure of functional *Staphylococcus aureus* alpha-hemolysin channels in tethered bilayer lipid membranes, Biophys. J. 96 (2009) 1547–1553.

[91] D.T. Bong, A. Janshoff, C. Steinem, M.R. Ghadiri, Membrane partitioning of the cleavage peptide in flock house virus, Biophys. J. 78 (2) (2000) 839–845.

[92] J. Dzubiella, J.M.J. Swanson, J.A. McCammon, Coupling hydrophobicity, dispersion, and electrostatics in continuum solvent models, Phys. Rev. Lett. 96 (Mar 2006) 087802.

[93] Mingyang Hu, John J. Briguglio, Markus Deserno, Determining the Gaussian curvature modulus of lipid membranes in simulations, Biophys. J. 102 (6) (2012) 1403–1410.

[94] Michael A. Heroux, Roscoe A. Bartlett, Vicki E. Howle, Robert J. Hoekstra, Jonathan J. Hu, Tamara G. Kolda, Richard B. Lehoucq, Kevin R. Long, Roger P. Pawlowski, Eric T. Phipps, Andrew G. Salinger, Heidi K. Thornquist, Ray S. Tuminaro, James M. Willenbring, Alan Williams, Kendall S. Stanley, An overview of the Trilinos project, ACM Trans. Math. Softw. 31 (3) (2005) 397–423.

[95] A.H. Baker, R.D. Falgout, Tz.V. Kolev, U.M. Yang, Scaling hypre's multigrid solvers to 100,000 cores, in: M. Berry, et al., (Eds.)High Performance Scientific Computing: Algorithms and Applications, 2012.

[96] Rio Yokota, Jaydeep P. Bardhan, Matthew G. Knepley, L.A. Barba, Tsuyoshi Hamada, Biomolecular electrostatics using a fast multipole BEM on up to 512 GPUs and a billion unknowns, Comput. Phys. Commun. 182 (6) (2011) 1272–1283.

[97] W. Śmigaj, S. Arridge, T. Betcke, J. Phillips, M. Schweiger, Solving Boundary Integral Problems With BEM++, http://www.bempp.org/files/bempp-toms-preprint.pdf (revised version).

[98] BrownFrank L.H. , Elastic modeling of biomembranes and lipid bilayers, Annu. Rev. Phys. Chem. 59 (2008) 685–712.

[99] H.I. Petrache, S.W. Dodd, M.F. Brown, Area per lipid and acyl length distributions in fluid phosphatidylcholines determined by (2)H NMR spectroscopy, Biophys. J. 79 (6) (2000) 3172–3192.

[100] Jianjun Pan, Frederick A. Heberle, Stephanie Tristram-Nagle, Michelle Szymanski, Mary Koepfinger, John Katsaras, Norbert Kučerkae, Molecular structures of fluid phase phosphatidylglycerol bilayers as determined by small angle neutron and X-ray scattering, Biochim. Biophys. Acta 1818 (9) (2012) 2135–2148.

[101] I.-M. Yu, H. Zhang, H.A. Holdaway, L. Li, V.A. Kostyuchenko, P.R. Chipman, R.J. Kuhn, M.G. Rossmann, J. Chen, Structure of the immature dengue virus at low pH primes proteolytic maturation, Science 319 (5871) (2008) 1834–1837.